Magnetization of high-density plasma with a jet velocity of hundreds of km/s

Tie-Huai Zhang,[1,3] Wei-Min Wang,[2,4,*] Yu-Tong Li,[1,3,4,5,†] and Jie Zhang[1,4,6]

[1]*Beijing National Laboratory for Condensed Matter Physics, Institute of Physics, CAS, Beijing 100190, China*

[2]*Department of Physics and Beijing Key Laboratory of Opto-electronic Functional Materials and Micro-nano Devices, Renmin University of China, Beijing 100872, China*

[3]*School of Physical Sciences, University of Chinese Academy of Sciences, Beijing 100049, China*

[4]*IFSA Collaborative Innovation Center, Shanghai Jiao Tong University, Shanghai 200240, China*

[5]*Songshan Lake Materials Laboratory, Dongguan, Guangdong 523808, China*

[6]*Key Laboratory for Laser Plasmas (MoE) and School of Physics and Astronomy, Shanghai Jiao Tong University, Shanghai 200240, China*

(Received 18 May 2022; accepted 1 November 2022; published 28 November 2022)

High magnetic fields at the kilotesla scale have been experimentally generated and finding methods to fully embed such fields into high-density plasma is interesting for magnetically assisted a fast ignition scheme of inertial confinement fusion, laboratory astrophysics, and magnetically guided fast electron beam for broad applications. We investigate diffusion and embedment of an external magnetic field inwards a high-density plasma by analysis and simulation. By introducing the magnetic Péclet number, dimensional analysis indicates that the magnetizing process is sensitive to the jet velocity, temperature, and size of the plasma and gives a phenomenological scaling law of the magnetic field embedment time with an arbitrary jet velocity. The analytical results are verified by magnetic field simulation and applied in 100-g/cm^3, 100-μm-radius plasmas with a jet velocity of 0–400 km/s and a temperature of 50–500 eV, typically adopted in experiments. Attributed to an effective electric field from frame transformation, the magnetic field embedment time can be significantly reduced by one order of magnitude when a jetting plasma is adopted with a velocity of hundreds of kilometers per second, e.g., from 5.5 ns in a static plasma to a 0.5 ns timescale in a jetting plasma of 200 km/s. The promoted embedment process favors for various applications mentioned above.

DOI: 10.1103/PhysRevE.106.055211

I. INTRODUCTION

Fast ignition (FI) [1–3], an important scheme of inertial confinement fusion (ICF), has been widely studied since the early 1990s due to its lower driven energy requirement in theory than the traditional central ignition ICF scheme [4,5]. Unlike the central ignition scheme, FI does not need the formation of a hot spot [6,7] but uses picosecond (ps) laser pulses to irradiate the compressed cold deuterium–tritium (DT) fuel and generate the fast electron beam (FEB), which is expected to heat the high-density plasma rapidly and create a spark for ignition. Nevertheless, experiments from different facilities [8–11] indicate that in the common FI scheme, the preplasmas formed by the picosecond laser prepulse would significantly enhance the divergence of the FEB, leading to an intolerable decrease on the energy coupling efficiency from the ps laser beam to the compressed target. Therefore, it is essential to restrain the FEB divergence in FI scheme. Apart from heating the compressed target in FI, FEB can be applied to generate intense K_α [12–15] and bremsstrahlung [16,17] x ray. Both of these radiation sources are applied to diagnostics in ICF and other detection fields extensively [18,19]. To raise the yield of x-ray radiation generated in the compressed plasma, an effective measure for constraining the divergent behavior and energy regime of FEB is also in demand.

Based on the requirements above, the magnetically assisted fast ignition (MAFI) schemes [20,21] and magnetically guided FEB [22] have gradually caught broad attention since the early 2010s. Loading an external strong magnetic field can alter the evolution process and transport characteristics in high-density plasma observably [23]. Previous works have proven that the strong magnetic field parallel to the ignition laser propagation direction can confine the macroscopic beam divergence angle of the FEB produced by picosecond pulses [20], create an ultra-high-energy-density state [24], and reduce the growth rate of Weibel instability [25]. In addition, in sufficiently magnetized plasma, the laser field can be converted to whistler mode [26–28], which can be applied to trigger thermonuclear fusion [29,30]. Additionally, a proper configuration of the external field can lower the impact on coupling efficiency caused by the magnetic mirror effect [21,31]. To achieve a higher transport efficiency of laser-driven FEB, various MAFI and other derivative schemes have been developed [21,30–32] and part of them have attained creditable results in experiments [33–37]. A neutron yield increase of 30% has been observed in the cylindrical spherical implosion experiment with seed magnetic fieldat the OMEGA Laser facility [34]. Over the past few years, significant progress has been made in the magnetized ICF field. The cylinder implosion experiment on OMEGA shows that

*weiminwang1@ruc.edu.cn

†ytli@iphy.ac.cn

an axial magnetic field at the optimal amplitude can increase the DD neutron yield by up to 44% [38], and extended-MHD simulations of both cylindrical and spherical implosion schemes reveal that enhancements of ion temperature in hot spot and neutron yield are approachable with the application of external B field [39–41]. Some recent works have also made detailed investigations into the features on electron transport in magnetized ICF scheme [35,36]. Fojioka *et al.* generated a magnetic field strength of 0.6 kT with a capacitor-coil target to guide FEB in the FIREX experiment, reaching a 10-fold boost in pciosecond pulse heating efficiency [37].

Although the external magnetic field is conducive to the transport process of FEB in high-density plasma in many aspects, its diffusion and embedment to the plasma interior requires a time period. In particular with MAFI, the time period from fuel compression to ignition is about 10 ns, which imposes limitations on magnetic field embedment. Embedding the magnetic field to the plasma too late would bring about a failure in the FEB transport into the high-density plasma, while premature generation of the strong external field could trigger new magnetohydrodynamic instabilities during fuel compression [42–45], and the vectorial property of magnetic field would broke the spherical symmetry in some scenarios of MAFI. Hence, for each specific MAFI scheme and magnetically guided FEB, a tailored field loading strategy is necessary. Recently, Zhang *et al.* proposed a double-cone ignition scheme [46] (DCI), where the guidance of the FEB by the external magnetic field is a crucial step. The fusion plasma in DCI and impact ignition [47] has a high jet velocity $u \sim 10^2$ km/s, so the evolution of magnetic field in both static and jetting plasma under an external field is worthy of studying.

In this article, we investigate the external magnetic field embedment and diffusion process in high-density plasma by analytic model and numerical simulation. Compared with the static plasma, the field embedding process in plasma with a high jet speed is dramatically expedited. When the plasma moves, the Lorentz term $\mathbf{u} \times \mathbf{B}$ appears in the transformation to the rest frame, leading to an effective electric field contributing to the ohmic current. Such an extra field can weaken the induced magnetic field, and the characteristic time of magnetization is eventually reduced from 5.5 to 0.5 ns in typical high-density plasma.

The article is organized as follows. In Sec. II, we begin with a simplified theoretical model based on the typical characteristics of laser-compressed plasma and give the general equations and self-consistent boundary conditions of magnetic diffusion under quasistatic approximation [48]. In Sec. III A, we attain an analytic solution in the case of spherical static plasma with $u = 0$ and show the features of magnetic field diffusion under typical parameters. To reveal the influence on evolution of magnetic field from jet velocity, a dimensionless number Pe_m is introduced in analogy with Péclet number in hydrodynamics. In Sec. III B, a jet velocity is taken into consideration, and a "magnetic convection term" is then added into the magnetic diffusion equation. With numerical simulation, we also compare the magnetic field loading behavior in typical high-density plasma with and without a jet velocity, demonstrating that the high jet velocity can strongly promote the loading process. In Sec. III C, to approach a more general temporal picture of external field penetration, a scaling relationship is developed for embedment time of magnetic field at the center of plasma. We obtain a phenomenological formula for an arbitrary Pe_m according to the asymptotic behavior of magnetic fields in the limit of both $\mathrm{Pe}_m \to 0^+$ and $\mathrm{Pe}_m \to +\infty$. Finally, it is the summary section.

II. ANALYTIC MODEL

To describe the issue addressed above, we suppose the following:

(a) Continuous medium hypothesis is valid in high-density regime, since we focus on magnetic field loading and do not take into account strong unequilibrium and nonlocal effects like fast electron transport. Thus, macro parameters like the electrical conductivity σ can describe the features of high-density plasma.

(b) The macroscopic flux can be ignored in the process of magnetic field diffusion, due to a quasispherical symmetry and its high density and high thermal pressure, which is far beyond the magnetic pressure $B^2/2\mu_0$ of the field generated by a coil target. Under this assumption, effects such as pressure, viscosity, and heat flow are omitted, i.e., fluid equations are not considered here. It is valid before the emergence of nonlinear hydrodynamic effects in the high-density region. Once the movement of plasma is decoupled from the electromagnetic field, the magnetic field can be normalized, inferring that the absolute value of the background field would not change the embedment behavior.

In the assumptions above, the high-density plasma can be regarded as a rigid nonideal conductor, whose magnetization process can be described with the Maxwell equations in the continuous medium.

For practical experiments in laboratory astrophysics and MAFI, a usual strategy to generate a strong kilotesla magnetic field is to use a nanosecond-pulse-driven capacitor-coil target [37,49,50], and Morita *et al.* [51] have researched the embedment process in gold cone of magnetic field generated by such a target in detail. Based on their results, the characteristic evolution time of the external field is $\Delta t \simeq 2$ ns, and the corresponding effective frequency and wavelength are $\omega \simeq 2\pi/\Delta t \simeq 10^9$/s and $\lambda \simeq 10$ cm, respectively. Consider typical parameters in FI, DCI, and laboratory astrophysics experiments, length of the high-density region $2a \simeq 2 \times 200$ μm, temperature $T_e = T_i \simeq 100$–500 eV, and mass density $\rho \simeq 100\ \mathrm{g/cm^3}$. With these parameters, the model can be further simplified.

First, because $2a \ll \lambda$, the displacement current in the background plasma can be omitted at any time, which means magnetostatic field equations are valid, i.e.,

$$\nabla \cdot \mathbf{B} = 0, \quad \nabla \times \mathbf{H} = \mathbf{0}. \tag{1}$$

Second, both the electron and ion plasma frequency $\omega_{\mathrm{pe}}, \omega_{\mathrm{pi}} \gg \omega$. The period of magnetic field is far longer than the characteristic time of the microscopic conduction. Furthermore, on account of the high density and low temperature, the electron free path is extremely short, which leads to the assumption that relationship between field and current is local. The current density $\mathbf{j}$ at an arbitrary point $\mathbf{r}_0$ only relies on the fields $\mathbf{B}(\mathbf{r}_0)$ and $\mathbf{E}(\mathbf{r}_0)$. Especially, in static plasma, one

can calculate the current density with the Ohm's law $\mathbf{j}(\mathbf{r}) = \sigma\mathbf{E}(\mathbf{r})$. Presume that the Spitzer formula [52],

$$\sigma = \frac{(4\pi\varepsilon_0)^2(k_B T_e)^{3/2}}{\pi Z e^2\sqrt{m_e}\ln\Lambda}, \tag{2}$$

is valid in the high-density plasma, where $\ln\Lambda$ is the Coulomb logarithm, Z is the average ionization of plasma, and T_e is the electron temperature. Under the typical parameters we can evaluate $\ln\Lambda = 5$ which is a "safe" value for the classical Spitzer-Harm (SH) formula and this treatment does not change the basic conclusion in our work, as shown in the discussion section. The conductivity ranges from 2.1×10^6 to 2.3×10^7 S/m, while the external field generated by the coil target gives the value $\omega\varepsilon_0 = 10^{-2}$–$10^{-1}$ S/m $\ll\sigma$. Therefore, the displacement current in high-density plasma can also be ignored.

When all the statements above are tenable, the field is quasistatic and the current in the high-density region obeys Ohm's law. In this case, we can use the pre-Maxwell equations,

$$\begin{aligned} &\nabla\cdot\mathbf{D} = 4\pi\rho, \quad \nabla\times\mathbf{E} = -\frac{\partial\mathbf{B}}{\partial t},\\ &\nabla\cdot\mathbf{B} = 0, \qquad \nabla\times\mathbf{H} = \mathbf{j}. \end{aligned} \tag{3}$$

Since the high-density plasma considered here is in the paramagnetic metallic fluid phase [53], the relative magnetic permeability μ_r can be viewed as identity, and the solenoidal condition is $\nabla\cdot\mathbf{B} = \mu\nabla\cdot\mathbf{H} = 0$. With Eq. (3), the well-known magnetic diffusion equation can be derived:

$$\eta\nabla^2\mathbf{H} = \frac{\partial\mathbf{H}}{\partial t}, \tag{4}$$

where $\eta = 1/\mu\sigma$ is the magnetic diffusivity and we regard it as a constant scalar in this ideal model. If the high-density plasma has a jet velocity $u \simeq 10^2$ km/s alone z axis, then the transformation of pre-Maxwell equations (3) from the laboratory to the rest frame [54] gives that

$$\mathbf{j}' = \sigma\mathbf{E}', \quad \mathbf{E}' = \gamma(\mathbf{E} + \mathbf{u}\times\mathbf{B}). \tag{5}$$

Due to the relativity factor $\beta = u/c \sim 10^{-3}$, $\gamma \simeq 1$, the relativistic effects can be ignored except for electric field $\mathbf{E}'$. For a constant speed $\mathbf{u} = u\hat{\mathbf{e}}_z$, $(\mathbf{H}\cdot\nabla)\mathbf{u} = \mathbf{H}(\nabla\cdot\mathbf{u}) = \mathbf{0}$ and in the rest frame we obtain the "magnetic convection-diffusion equation,"

$$\frac{\partial\mathbf{H}'}{\partial t} + (\mathbf{u}\cdot\nabla)\mathbf{H}' = \eta\nabla^2\mathbf{H}', \tag{6}$$

and its boundary condition $\mathbf{n}\times[\mathbf{H}'^{(e)} - \mathbf{H}'^{(i)}] = \mathbf{j}_s'$, $\mathbf{n}\cdot[\mathbf{B}'^{(e)} - \mathbf{B}'^{(i)}] = 0$ becomes time independent. Here the superscripts "e" and "i" denote the external and internal field, $\mathbf{j}_s'$ is the surface current density, $\mathbf{n}$ is normal vector of the boundary surface of high-density region, and the prime marks a physical quantity in the rest frame. If not particularly indicated, then the discussion will be limited in the rest frame and all the primes will be omitted in the rest of this article. For typical high-density plasma, the skin depth $\delta = 1/\mathrm{Re}\sqrt{\mathbb{i}\omega\mu(\sigma + \mathbb{i}\omega\varepsilon)} \simeq 11.9$ μm, which suggests that the induced current does not concentrate on the surface and $\mathbf{j}_s$ can be ignored. The boundary condition finally becomes $\mathbf{H}^{(e)} = \mathbf{H}^{(i)}$.

It should be noted that the embedment process of B field in plasma could be more complicated, which requires systematic and extended MHD simulations [40,55,56]. Equation (6) only contains resistive diffusion (with a static isotropous conductivity) and advection of a uniform bulk jet velocity.

In this case, we assume a spherical symmetry of high-density region with a radius of a. Because of the nonzero values of Christoffel symbols Γ^k_{ij} in spherical coordinate, components of field are coupled in Eq. (4) and Eq. (6), making the problem much more difficult than the convection-diffusion process of a scalar field. To describe the magnetic field within the high-density region, we introduce the toroidal-poloidal decomposition (TPD) method commonly used in tokamak and dynamo research [57]. According to the Helmholtz-Hodge decomposition theorem, a smooth nondivergent vector field $\mathbf{H} = \mathbf{T} + \mathbf{P}$ can be divided into a poloidal field $\mathbf{P}$ and a toroidal field $\mathbf{T}$. In the spherical coordinate, the two fields can be expressed as

$$\mathbf{T} = \nabla\times(\mathbf{r}T), \quad \mathbf{P} = \nabla\times\nabla\times(\mathbf{r}S), \tag{7}$$

where $\mathbf{r} = r\hat{\mathbf{e}}_r$ is position vector and $T = T(r,\theta,\varphi)$, $S = S(r,\theta,\varphi)$ are scalar fields.

The same decomposition can be applied to a nondivergent vector field $\mathbf{v} = \mathbf{t} + \mathbf{p}$, $\mathbf{t} = \nabla\times(\mathbf{r}\mathscr{t})$, $\mathbf{p} = \nabla\times\nabla\times(\mathbf{r}\mathscr{s})$. After tedious vector and tensor differential calculation, the well-known Bullard-Gellman equations [58] is obtained:

$$\begin{aligned}(\partial_t - \eta D_\gamma)S_\gamma = &\sum_{\alpha,\beta}[(\mathscr{s}_\alpha, S_\beta, S_\gamma) + (\mathscr{s}_\alpha, T_\beta, S_\gamma)\\ &+(\mathscr{t}_\alpha, S_\beta, S_\gamma) + (\mathscr{t}_\alpha, T_\beta, S_\gamma)], \end{aligned} \tag{8a}$$

$$\begin{aligned}(\partial_t - \eta D_\gamma)T_\gamma = &\sum_{\alpha,\beta}[(\mathscr{s}_\alpha, S_\beta, T_\gamma) + (\mathscr{s}_\alpha, T_\beta, T_\gamma)\\ &+(\mathscr{t}_\alpha, S_\beta, T_\gamma) + (\mathscr{t}_\alpha, T_\beta, T_\gamma)]. \end{aligned} \tag{8b}$$

The subscripts γ represents for the (l_γ, m_γ) coefficient of spherical harmonics and radical differential notation $D_\gamma = \partial_r^2 + (2/r)\partial_r - l_\gamma(l_\gamma+1)/r$. The parenthesis terms on the right-hand sides of Eqs. (8a) and (8b) are TPD spectral interaction terms, which have been discussed in Ref. [57].

Besides, the magnetic polarization cannot be ignored near the surface of high-density plasma, it is essential to take the change of background magnetic field into consideration. Equation (1) suggests that we can introduce a magnetic scalar potential ϕ to describe the field in the background plasma. We suppose that $\mathbf{H}^{(e)}$ has the form of $\mathbf{H}^{(e)} = -\nabla\phi(\mathbf{r},t) + \mathbf{H}_\infty$, and $\phi = 0$, $\nabla\phi = 0$ at the limit of $|\mathbf{r}|\to\infty$. Considering that the external magnetic field is generated by the coil target, whose radius is much larger than the width of typical high-density region, the magnetic field at infinity is close to uniform along the x axis: $\mathbf{H}(r\to\infty) = \mathbf{H}_\infty(t) = H_\infty(t)\hat{\mathbf{e}}_x = H_\infty(t)(\sin\theta\cos\varphi\hat{\mathbf{e}}_r + \cos\theta\cos\varphi\hat{\mathbf{e}}_\theta - \sin\varphi\hat{\mathbf{e}}_\varphi)$. The plasma has a uniform velocity of $\mathbf{u} = u\hat{\mathbf{e}}_z = u(\cos\theta\hat{\mathbf{e}}_r - \sin\theta\hat{\mathbf{e}}_\theta)$. With the spherical harmonic expansion of potential $S = \sum_{l,m} S_l^m(r)Y_l^m(\theta,\varphi)$, $T = \sum_{l,m} T_l^m(r)Y_l^m(\theta,\varphi)$ as well as

$\phi = \sum_{l,m} \phi_l^m(r) Y_l^m(\theta, \varphi)$, we obtain the self-consistent boundary conditions of their components S_l^m and T_l^m at $r = a$, which denote the coefficients of spherical harmonics Y_l^m. We present the detailed derivation in Appendix A and give the results:

$$T_l^m\big|_{r=a} = 0, \tag{9a}$$

$$\left[\frac{a}{l+1}\frac{\partial S_l^m}{\partial r} + S_l^m\right]_{r=a} = \begin{cases} 0, & (l,m) \neq (1,\pm 1) \\ -\frac{\sqrt{6}ma}{8} H_\infty(t), & (l,m) = (1,\pm 1) \end{cases}. \tag{9b}$$

Notice that these boundary conditions are based on the quasistatic approximation, the boundary field configuration, and the geometry assumption.

We set that there is no magnetic field in high-density plasma at $t = 0$. The initial value of TPD coefficients $S_l^m(r < a)$, $T_l^m(r < a)$ are zeros, and the initial external field can be expressed with $H_{\infty 0} = H_\infty(t = 0)$:

$$\mathbf{H}_0^{(e)} = H_{\infty 0}\hat{\mathbf{e}}_x - \frac{H_{\infty 0}}{2}\left(\frac{a}{r}\right)^3 (2\sin\theta\cos\varphi\hat{\mathbf{e}}_r - \cos\theta\cos\varphi\hat{\mathbf{e}}_\theta + \sin\varphi\hat{\mathbf{e}}_\varphi). \tag{10}$$

Once the temporal variable $H_\infty(t)$ has an explicit form, Eqs. (8a), (8b), (9a), and (9b) give a unique solution, which can be solved numerically.

III. EVALUATION IN STATIC AND JETTING PLASMA

A. Static plasma

First, we focus on the condition of $\mathbf{u} = \mathbf{0}$ in static plasma, where Eq. (6) degenerates to Eq. (4), and all of the coupling terms on the right-hand sides of Eqs. (8a) and (8b) are vanished, i.e., the spectral interaction equations are decoupled. Due to the form of (9a) and (9b), for any T_l^m and S_l^m with $(l,m) \neq (1,\pm 1)$, both the equation and boundary conditions are homogeneous, resulting in a trivial solution. For $S_1^{\pm 1}$, nondimensionalizing this problem with $\tilde{r} = r/a, \tilde{t} = t/(a^2\eta^{-1})$, the solution is given by Eq. (11), where j_ν represents for the spherical Bessel function of the order ν and the tilde symbol signs a dimensionless variable,

$$S_1^{\pm 1} = \mp\left[\frac{H_\infty(\tilde{t})}{2\sqrt{6}} a\tilde{r} + \frac{a}{2\sqrt{6}}\sum_{n=1} C_n(\tilde{t})\frac{j_1(n\pi\tilde{r})}{n\pi}\right], \tag{11}$$

where

$$C_n(\tilde{t}) = (-1)^n \cdot 6e^{-(n\pi)^2\tilde{t}} \times \left[H_{\infty 0} + \int_0^{\tilde{t}} H'_{\infty 0}(\tilde{\tau}) e^{(n\pi)^2\tilde{\tau}} d\tilde{\tau}\right].$$

Substituting the results in Eq. (11) into Eq. (7), one can obtain the the components of magnetic field in the high-density region:

$$\begin{aligned} H_r &= \cos\varphi\sin\theta\left[H_\infty(\tilde{t}) + \sum_{n=1} C_n(\tilde{t})\frac{j_1(n\pi\tilde{r})}{n\pi\tilde{r}}\right] \\ H_\theta &= \cos\varphi\cos\theta\left\{H_\infty(\tilde{t}) + \sum_{n=1}\frac{C_n(\tilde{t})}{2}\left[j_0(n\pi\tilde{r}) - \frac{j_1(n\pi\tilde{r})}{n\pi\tilde{r}}\right]\right\} \\ H_\varphi &= -\sin\varphi\left\{H_\infty(\tilde{t}) + \sum_{n=1}\frac{C_n(\tilde{t})}{2}\left[j_0(n\pi\tilde{r}) - \frac{j_1(n\pi\tilde{r})}{n\pi\tilde{r}}\right]\right\}. \end{aligned} \tag{12}$$

To grasp a clearer picture of the diffusion process, we inspect a special case where $H_\infty(t) \equiv H_{\infty 0} = H_{\text{back}}$. The convolution term will vanish and the magnetic field inside high-density plasma will be consistent with the background field H_{back} at infinity points eventually. For the field generated by a coil target, such a steady background field assumption is appropriate around the plateau of field strength. Under the irradiation of a nanosecond pulse, such a plateau lasts for approximately 0.5 ns, shown in Ref. [51]. Unless indicated otherwise, we always consider the field at infinite point time independent for simplicity. We calculate the first 40 terms of the series in Eq. (12) with the typical parameter values mentioned in Sec. II, and plot the temporal evolution of the field component H_x in Fig. 1(a) and the strength of H_x along the x axis with $k_BT = 100$ eV in Fig. 1(b).

The timescale of field embedding into the center of plasma is around 10 ns, which is close to the compression laser beam duration in ICF. Apart from that, the dimensional analysis gives that the characteristic time of diffusion $\Delta t = a^2/\eta \propto a^2 T^{3/2}$, indicating that the diffusion process is significantly sensitive to the temperature of plasma. Actually, increasing the temperature to $k_BT = 500$ eV, 61 ns is needed for H_x at central point reaching $0.75H_{\text{back}}$, which is far longer than typical ICF implosion time. Hence, for plasma with high temperature, embedding magnetic field needs to be in advance of compression for MAFI or DCI, which is unfavorable. If the Spitzer formula (2) still works, then a sufficient low temperature or an extremely low preheating is indispensable for the magnetically guiding of FEB generated by the picosecond laser pulse. Note that comparing with Ref. [51], we do not consider the time evolution of electric conductivity due to ohmic heating during the magnetic diffusion process, which requires a detailed calculation of the equation of states of the cold dense DT plasma.

B. Plasma with a jet velocity

When the plasma has a jet velocity $\mathbf{u}$, the convection effect starts to appear. In the usual convection-diffusion equation, Péclet number (Pe) is a fundamental dimensionless number which describes the ratio of convection and diffusion transport speed. Here we introduce the magnetic Péclet number Pe_m as in Eq. (13) with a similar definition,

$$\text{Pe}_m \equiv au/\eta = \mu_0\sigma au \propto \sigma au. \tag{13}$$

Substituting $a = 100$ μm, $u = 200$ km/s, and $k_BT = 100$ eV into (13), we obtain $\text{Pe}_m = 51.849$, which suggests that the magnetic "convection" takes a dominant position.

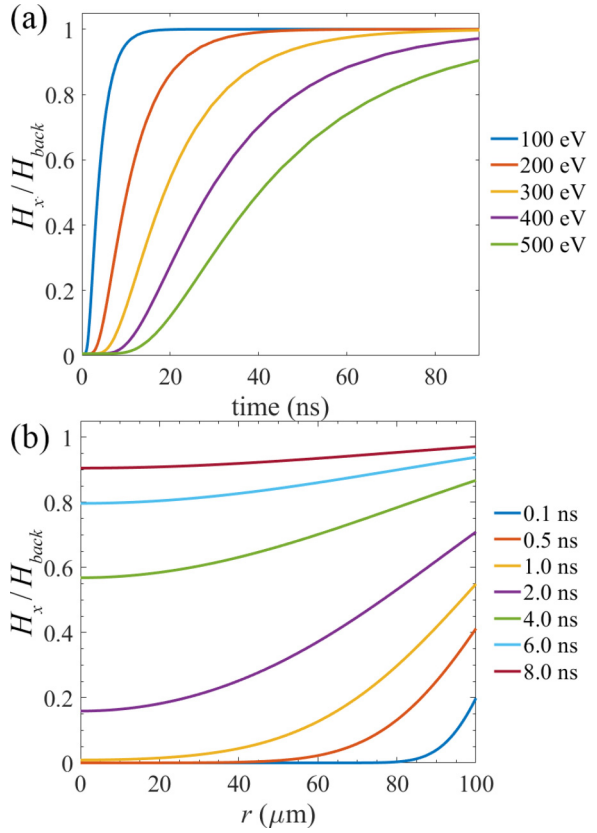

FIG. 1. (a) The temporal evolution of the magnetic field H_x at the plasma center with temperature k_BT varied from 100 to 500 eV (corresponding to the curves with different colors). (b) The distribution of H_x along the x axis with $k_BT = 100$ eV at different moments (corresponding to the curves with different colors).

Redefine $\tilde{t} = t/(au^{-1})$, and the dimensionless form of Eq. (6) is given by

$$\frac{\partial \mathbf{H}}{\partial \tilde{t}} + (\tilde{\mathbf{u}} \cdot \tilde{\nabla})\mathbf{H} = \mathrm{Pe}_m^{-1}\tilde{\nabla}^2\mathbf{H}. \tag{14}$$

With a steady jet velocity, $\tilde{\mathbf{u}} = \hat{\mathbf{u}}$ is the unit vector. To attain a numerical solution of Eq. (14), the complex calculation of the coupling terms in Bullard-Gellman equations is inevitable. Fortunately, when the jet velocity $\mathbf{u} = u\hat{\mathbf{e}}_z$ is steady, it is easy to verify that the TPD of $\mathbf{u}$ is $\mathfrak{d}(r < a) = (ur\cos\theta)/2 = urY_1^0/2\sqrt{3}$, $\mathfrak{t}(r < a) \equiv 0$, leading to zero values of those coupling terms except for $(\mathfrak{d}_1^0, S_\beta, S_\gamma)$, $(\mathfrak{d}_1^0, T_\beta, S_\gamma)$, $(\mathfrak{d}_1^0, S_\beta, T_\gamma)$, and $(\mathfrak{d}_1^0, T_\beta, T_\gamma)$. After lengthy calculations, it is confirmed that Eq. (8a) and Eq. (8b) can be simplified to two sets of cascade equations (S_l^1, T_l^1), (S_l^{-1}, T_l^{-1}) containing infinite unknown scalar functions where $l \in \mathbb{N}^*$. The cascade structure of the simplified equations is shown in Fig. 2, and the accurate form of these equations is given in Appendix B.

Even though the velocity $\mathbf{u}$ is fixed, it is hard to obtain an analytical solution of those equations. Here we investigate the jetting plasma by simulations. The simulation domain is a sphere with the radius of $3a = 300$ μm, and the high-density plasma is located at the center cut at a sphere with $r \leqslant a$. We take $\sigma_p = 2.06 \times 10^6$ S/m (corresponding to $k_BT = 100$ eV) and $\mathbf{u} = u\hat{\mathbf{e}}_z$. The background electric conductivity is set to $\sigma_b = 0.1$ S/m for the rest of domain. Based on Eq. (10), the

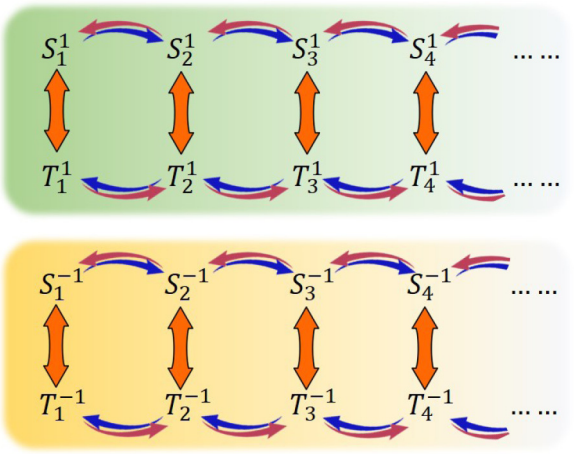

FIG. 2. The cascade structure of coefficients of TPD when the spherical plasma has a uniform velocity $\mathbf{u} = u\hat{\mathbf{e}}_z$

induced field in the background shell is proportional to $(a/r)^3$ and has a ignorable strength of $\sim 0.037H_{\mathrm{back}}$ at $r = 3a$. Hence, we set the boundary field $\mathbf{H}^{(e)}(r = 3a) = H_{\mathrm{back}}\hat{\mathbf{e}}_x$ directly and the initial values $\mathbf{H}^{(i)}(t = 0) \equiv \mathbf{0}$ and $\mathbf{H}^{(e)}$ as Eq. (10). It should be noticed that simulations which we present in this article also use a rigid conductor model, which means that the conductivity keeps uniform and static and no MHD physics except the resistive diffusion and the advection of bulk plasma is considered here. Figure 3 shows the temporal evolution of magnetic field at different positions in the high-density region with both $u = 0$ and $u = 200$ km/s. For comparison, other parameters are set identically. The convection effect strongly promotes magnetic field embedment and reduces the time cost for magnetic field embedded at central point reaching 75%

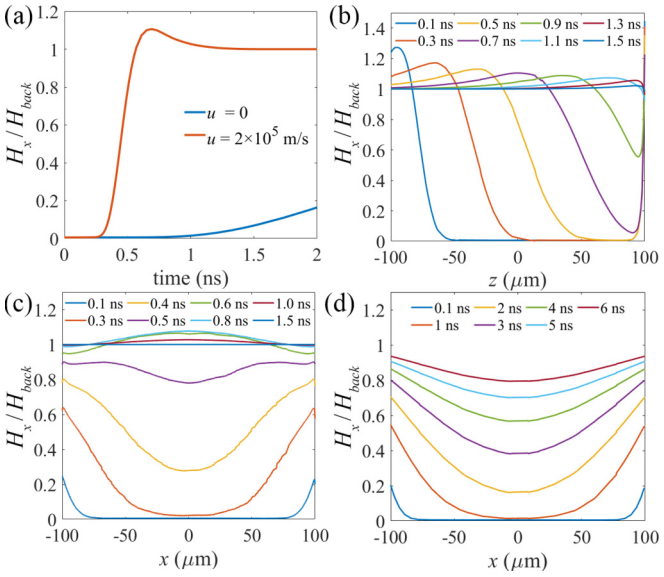

FIG. 3. (a) The normalized magnetic field H_x/H_{back} at the center of plasma with $u = 0$ and $u = 200$ km/s, respectively. (b) Distribution of H_x/H_{back} on z axis with $u = 200$ km/s at different moments. The temporal evolution of H_x/H_{back} on x axis with the jet velocity (c) $u = 200$ km/s and (d) $u = 0$.

H_{back} from 5.5 ns (with $u = 0$) to ~0.5 ns [$u = 200$ km/s, as observed in Fig. 3(a)]. Figure 3(b) indicates that the temporal evolution of magnetic field H_x parallel to the jet velocity is similar with a normal convection-diffusion system of a scalar field in hydrodynamics. The field is "propelled" along the $+z$ direction, and the induced magnetic field caused by surface effect is smoothed gradually.

The analytical solution in Sec. III A is consistent with results in Fig. 3(d), while the evolution shown in Fig. 3(c) varies greatly due to the high jet velocity. Although the magnetization processes are similar at the early stage ($t \leqslant 0.1$ ns), the field strength at the center of plasma with $u = 200$ km/s soars dramatically from $t = 0.3$ to 0.6 ns, much faster than the steady situation. Such a distinction can be ascribed to the rapid move of the "magnetic diffusion front" shown in 3(b), which reaches the plasma center at around 0.3 ns. Combining Figs. 3(b), 3(c) and 3(d), it can be confirmed that "convection" rather than diffusion process primarily contributes to the rapid rise of H_x.

This phenomenon can be explained qualitatively as follows. When the spherical plasma is static, the current in the high-density region is a bunch of loops flowing clockwise around $+x$ axis in the yOz plane, generating a induced field to impede the external magnetic field embedment. However, once the plasma has a jet velocity $\mathbf{u} = u\hat{\mathbf{e}}_z$, according to Eq. (5), an equivalent additional electric field $\mathbf{u} \times \mathbf{B}$ appears in the rest frame, which is along the $+\hat{\mathbf{e}}_y$ direction. The equivalent electric field would weaken the induced current where $j_y < 0$ and strengthen it where $j_y > 0$. Therefore, the induced current loops are squeezed to the $+z$ side of the high-density region and the magnetic field can embed from $-z$ toward the $+z$ direction.

Typical magnetic field distributions in the high-density region with $u = 200$ km/s and $u = 0$ are also plotted in Fig. 4. When the plasma stays static, the system has a rotational symmetry and magnetic field along x axis has the x component only. However, the jet velocity along the z direction breaks this symmetry, leading to the twist of magnetic field lines on x axis. Such twist takes place mainly at the magnetic diffusion front and then flattened in the further evolution. Concentrating on the angle between the field and x axis at point $(a/2, 0, 0)$, the maximum value can reach ~27°, then decays near to zero in the following 1 ns.

In the whole simulation, the maximum strength of magnetic field $|\mathbf{H}| \simeq 1.5H_{\text{back}}$. The magnetic field lines near the plasma surface are twisted and compressed due to the curved boundary, as shown in Fig. 4. If we take $B_0 \equiv H_{\text{back}}/\mu_0 = 1000$ T (a typical field magnitude generated by coil targets), then the magnetic pressure $p_m = B_0^2/2\mu_0 = 8.95$ Mbar, which is far lower than the typical ICF target thermal pressure (~10^2 Gbar) in the ignition phase. Therefore, it is reasonable to ignore the influence of magnetic field on dynamic evolution of high-density plasma jet flow, verifying the rationality of assumption (b) in Sec. II.

C. Scaling law of the magnetic field embedment time

Assuming that the magnetic field at the infinite point is still uniform and time independent, we evaluate the embedment time of the magnetic field into the plasma center. We select

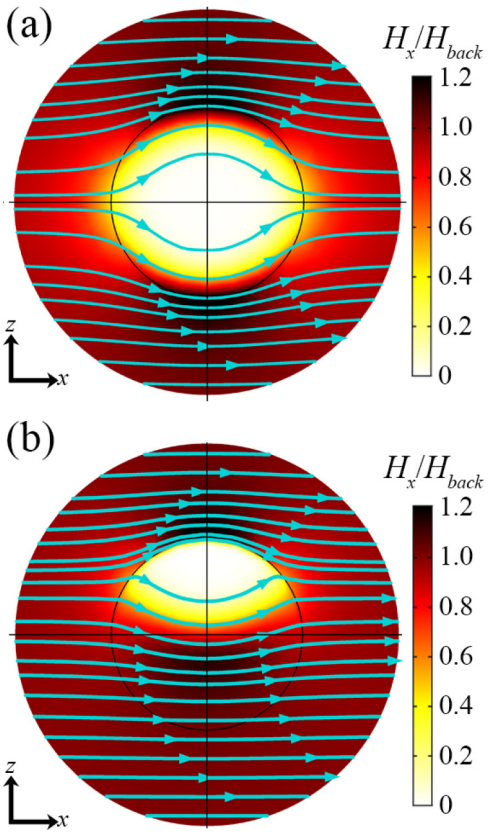

FIG. 4. The strength distribution of H_x/H_{back} and the magnetic field lines on xOz plane with (a) $u = 0$ and (b) $u = 200$ km/s at $t = 0.5$ ns. The two concentric circles represent for $r = a$ (boundary of high-density region) and $r = 2a$ separately.

the embedment time as the moment of H_x reaching $0.75H_{\text{back}}$, the average of the initial strength inside and outside the plasma surface at $r = a, \theta = 0$, given by Eq. (10), as a characteristic parameter, which is marked by $t_{0.75}$.

In the static plasma, the field at $r = 0$ has an analytical solution according to Eq. (12). Letting $r \to 0$, the solution has a simple form of $H_x(t) = H_{\text{back}}\vartheta_4[\exp(-\pi^2 t/a^2\mu_0\sigma)]$, where ϑ_4 represents for the fourth elliptic theta function. When $t/a^2\mu_0\sigma > 1$, there is a expansion of $H_x(t) \approx 1 - 2\exp(-2\pi^2 t/a^2\mu_0\sigma) + 2\exp(-4\pi^2 t/a^2\mu_0\sigma)$, giving the result

$$t_{0.75} = 0.210\mu_0\sigma a^2 = 0.086\frac{T_e(\text{keV})^{3/2}a(\mu\text{m})^2}{Z\ln\Lambda}(\text{ns}), \quad (15)$$

where Eq. (2) has been applied. As the plasma temperature and scale rise, the time for magnetic field embedding to the center increases. Note that such a relationship is determined by the general property of the solution to a diffusion equation, which means it may be applicable for high-density plasma even with an irregular boundary geometry, where the coefficient 0.210 should be slightly adjusted.

With respect to the jetting plasma, according to the nondimensionalization of the Bullard-Gellman equations [Eqs. (8a) and (8b)] and boundary conditions [Eqs. (9a) and (9a)], it is obvious that the solution is only related to the dimensionless number $\text{Pe}_m = \mu_0\sigma au$. Figure 5(a) shows that the embedding time increases rapidly with the growth of Pe_m. For the typical

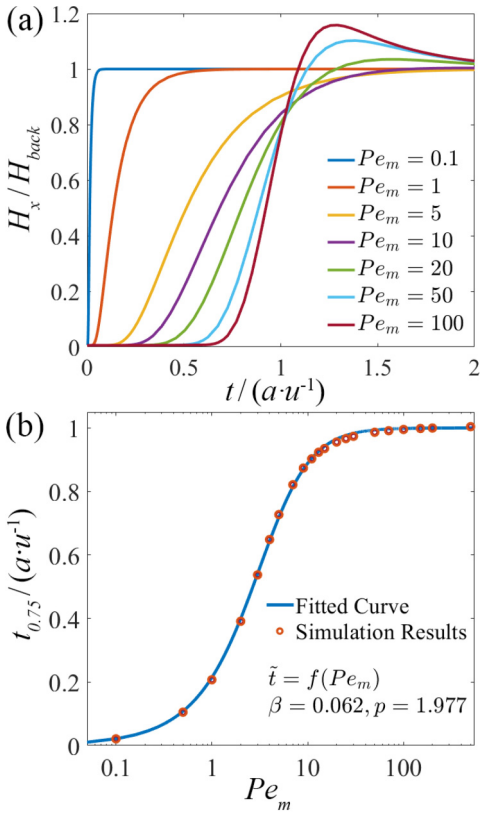

FIG. 5. (a) Temporal evolution of H_x/H_{back} at the plasma center with different Pe_ms. The horizontal axis is $t/(a\cdot u^{-1})$, where u is the jet velocity. (b) Fitted curve of normalized time when the magnetic field at the plasma center reaches $0.75H_{\text{back}}$ with different Pe_ms.

high-density jetting plasma, $\text{Pe}_m \sim 50$ is much larger than identity, corresponding to $t_{0.75} = 0.986a/u$. The peak value of normalized H_x is larger than identity when Pe_m is above $\sim$10, which attributes to the weak diffusion process. That is, the strong field generated by boundary effect has no time to be flattened because of the relatively high jet speed. We set $t_{0.75}/(au^{-1}) = f(\text{Pe}_m)$ and discuss the asymptotic behavior of $f(\text{Pe}_m)$ as follows.

On the one hand, when $\text{Pe}_m \to +\infty$, the convection term dominates the evolution process, and the right-hand side of Eq. (6) can be omitted. The equation becomes the following:

$$\frac{\partial \mathbf{H}}{\partial t} + (\mathbf{u}\cdot\nabla)\mathbf{H} \equiv \frac{d\mathbf{H}}{dt} = \mathbf{0}. \tag{16}$$

Then Eq. (16) has a trivial solution $\mathbf{H}(\mathbf{x}, t) = \mathbf{H}_0(\mathbf{x} - \mathbf{u}t)$. Normalized time for the external field reaching the center is $t/(au^{-1}) = f(\text{Pe}_m \to +\infty) = 1$. It should be noted that in this limit, the typical plasma parameters $a = 100$ μm and $u = 200$ km/s result in a lower limit for embedment of 250 ps, 22 times shorter than time spent in the $u = 0$ limit.

On the other hand, $\text{Pe}_m \to 0$ means that the convection term can be ignored, the governing equation degenerates to Eq. (4), and the solution comes back to Eq. (15), where $t_{0.75}/(au^{-1}) = 0.210\mu_0\sigma a^2/(au^{-1}) = 0.210\,\mu_0\sigma au = 0.210\text{Pe}_m$. Thus, $f(\text{Pe}_m \to 0^+) = \alpha\text{Pe}_m$, where $\alpha = 0.210$ is given by the analytical solution (15).

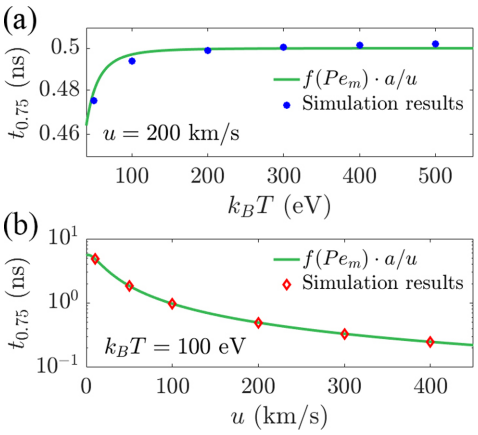

FIG. 6. $t_{0.75}$s of (a) different plasma temperatures with the same jet velocity $u = 200$ km/s, and (b) different jet velocity with the same plasma temperature $k_BT = 100$ eV, in comparison with the fitting formula (17). The y axis is $t_{0.75}$, and the x axis represents k_BT and u separately. The radius of the high-density region is fixed at $a = 100$ μm and the Coulomb logarithm $\ln\Lambda$ takes the constant value of 5.

We obtain $t_{0.75}$s under different Pe_ms by use of COMSOL code. Based on the growth characteristics of $t_{0.75}$ and the asymptotic behaviors given above, we suppose that the data are subject to a phenomenological formula,

$$f(\text{Pe}_m) = t_{0.75}/(au^{-1}) = 1 - \frac{1}{1 + \alpha\text{Pe}_m + \beta(\text{Pe}_m)^p}, \quad p > 1, \tag{17}$$

where $\alpha = 0.210$ is given by Eq. (15). One can verify the asymptotic behaviors by expanding Eq. (17) in Taylor series at $\text{Pe}_m = 0$ and $\text{Pe}_m \to +\infty$. Fitting the $t_{0.75}$ data with Eq. (17), it turns out that $\beta = 0.062$ and $p = 1.977$. The fitted curve and original data points are shown in Fig. 5, where the maximum residual error is 0.01 (at $\text{Pe}_m = 25$). For an arbitrary Pe_m, one can get the characteristic time of magnetic field embedment with Eq. (17) directly, where α, β, and p depend on the boundary geometry only. Notice that $t_{0.75}(\text{Pe}_m > 20)$ is larger than $0.95a/u$ in Fig. 5(b). For the typical high-density plasma discussed in this article, $\text{Pe}_m \simeq 50$ and it is enough to estimate the embedment time with $t_{0.75} \sim a/u$.

By substituting different plasma parameters into Eq. (17), we can get insight into the dependence of $t_{0.75}$ on both temperature and jet velocity. Figure 6 compares results from simulation and the fitting formula (17), with a fixed radius of $a = 100\mu m$. With a high jet velocity of $u = 200$ km/s, the embedment time changes little (less than 0.03 ns) where the temperature varies from 50 to 500 eV. However, $t_{0.75}$ decreases rapidly with the rise of jet velocity where k_BT is fixed at 100 eV; $t_{0.75}$ with a jet velocity $u = 10$ km/s is 20 times larger than the value of $u = 400$ km/s.

It should be noted that quantum effects would play a role in electric conductivity calculation when the temperature of high-density plasma is extremely low, which could lead to a change in the curve in Fig. 6(a). Actually, all of the results above are based on the Spitzer electric conductivity formula (2), while for experimental

high-density plasma with $\rho \sim 100$ g/cm^3 and $k_BT \sim 100$ eV, the Fermi temperature of electrons is $k_BT_F = (3\pi^2\rho/M)^{2/3} \cdot \hbar^2/2m_e \sim 300$ eV and the Coulomb-coupling constant $\Gamma = e^2/4\pi\varepsilon_0(3M/4\pi\rho)^{1/3}k_BT \sim 0.67$, where M is the average atomic mass of DT fuel. Therefore, quantum degeneracy could modify the Spitzer conductivity of plasma in Eq. (2) to some degree. When $T/T_F \geqslant 0.1$ and $\Gamma \leqslant 2$, the generalized Coulomb logarithm $\ln\Lambda$ can be applied to the modification of conductivity formula [59]. $\ln\Lambda$ falls rapidly with the decrease of T at low temperature, and σ no longer varies with $T^{3/2}$, where the classical SH formula is no longer valid. When the plasma is at a high-density and low-temperature state, the modification of Coulomb logarithm and transport coefficients can vary greatly depending on different existing models and methods [59–62]. In this work, we have taken the Coulomb logarithm as $\ln\Lambda = 5$, a "safe" value for the classical SH formula. This value is somewhat larger than the one calculated with the plasma temperature and density, but the influence on our results is not significant because $\ln\Lambda$ and the quantum effects would only affect electric conductivity σ in this model. When the plasma state becomes further away from the classical limit, σ is larger than the value given by SH formula, leading to a weaker resistive diffusion of B field. However, larger σ leads to a higher Pe_m value ($\mathrm{Pe}_m \propto \sigma$), which makes the drifting effect stronger. According to Eq. (17), one can find that the increased σ causes little influence on the B-field embedment time in the jetting plasma. Another effect worthy of investigation is the expansion of plasma. In fact, considering the velocity variation and compressibility of plasma, there are two extra terms, $-\mathbf{H}(\nabla\cdot\mathbf{v})$ and $(\mathbf{H}\cdot\nabla)\mathbf{v}$, on the right-hand side of Eq. (6). For usual SDP jet in free space, $-\rho\nabla\cdot\mathbf{v} = d\rho/dt < 0$, implying that the expansion process might play a negative role in magnetic field penetration.

The MHD effects could alter the magnetic field evolution process. To self-consistently consider the MHD effects such as Nernst effect and Hall effect, a systematic and extended MHD simulation is demanded, which is beyond the research regime of this work. Here a qualitative discussion is presented to evaluate the strength of these MHD effects in our case. First, we can evaluate the influence of the Hall term with Hall parameter [43]:

$$\omega_c\tau_{ei} \simeq 1.3(B/100\ \mathrm{T})(T_e/100\ \mathrm{eV})^{3/2}(n_e/10^{21}\ \mathrm{cm}^{-3})^{-1}, \tag{18}$$

In magnetized ICF, due to the high temperature (∼keV) and low density of the hot spot during stagnation, the Hall parameter can rise much higher than unity under the compressed B field (∼kT). Therefore, the Hall term is significant to thermal conduction and magnetic field transport. However, in the DCI scheme, the plasma around target center is designed to be compressed to a low-temperature (∼100 eV) and high-density (∼100 g/cm^3) state, where the Hall parameter is $\omega_c\tau_{ei} \sim 10^{-3} \ll 1$. Therefore, we consider the Hall effect as a less important factor on magnetic field transport in the configuration in our work. Second, under such plasma conditions, the resistive diffusion predominates instead of Nernst advection [56] and the cross-gradient-Nernst coefficient is also much smaller than unity [55]. Therefore, one can expect that these extended effects would bring a limited influence on the B-field embedment process in our case. Besides, the mismatch of gradients of temperature, density, and ion charge state usually exists, which would lead to self-generated magnetic fields (Biermann effect) [56,63]. Our investigation is limited in magnetic field embedment to a plasma with relatively low temperature, where the temperature gradient should be low and the self-generated field would not influence the primary picture of external field transport. Note that the jet velocity discussed in this article might lead to new instabilities and amplify these extended-MHD effects. For example, the equivalent electric field can change the distribution of induced current, which would make the thermal transport effects emerge. To examine these possible effects, further investigations with MHD simulation are demanded.

IV. CONCLUSION

In summary, we have investigated the evolution and embedment of an external magnetic field inward high-density spherical plasma with analytical and numerical methods. Based on the rigid conductor model and quasistatic field approximation, we have derived the equations for the magnetic field evolution and obtained the temporal solutions for static and jetting plasma. For an arbitrary jet velocity u, a general scalar relationship is presented. It is shown that jet velocity of the 100-km/s scale can significantly promote the process of field penetration and shorten the magnetization time of typical high-density plasma in practical experiments, e.g., the magnetization time can be reduced from 5.5 to 0.5 ns when the jet velocity is changed from 0 to 200 km/s. The analytic results are verified by simulation.

In this work, the diffusion process is based on a given extern magnetic field initially distributed outside of a plasma; therefore, our investigation does not depend on the generation route of the magnetic field. Furthermore, because our analysis and calculations are based on a linear model, the strength of the extern magnetic field would not change the embedment time and normalized field configuration, i.e., even if the kT-scale magnetic field cannot be generated, there is little influence on the main conclusions. This model can be considered valid before the emergence of nonlinear effects of hydrodynamics. Fortunately, it should be enough for our topic because as the hydrodynamic processes such as blow-out become obvious, the high-density region could also break down.

It should be noticed that we take the plasma with a density around ∼100 g/cm^3, a temperature of hundreds of eV, a jet velocity of hundreds of km/s, and the jet velocity is perpendicular to the extern B field, which is mainly according to the design as well as our experimental results in the double-cone ignition scheme [46]. Also, the results of embedment time could be referred by the laboratory astrophysics research related to magnetized plasma (such as Ref. [50]). The investigation might be partially applicable to the magnetized ICF [38,42] at the beginning stage when the plasma temperature is as low as hundreds of eV. But it should not completely applicable because the B field could not always be uniform and perpendicular to the implosion velocity of the plasmas in the whole space.

Note that finding a method to accurately measure the magnetic fields in the laser-driven coil targets is still a challenge [64]. Different diagnostic methods have been applied to the measurement of B field from coil target [65–67], showing that the result is related to the target configuration, material, diagnostic method, etc. Although the significant confinement and collimation of MeV electron beams and enhanced target heating experimentally observed in Refs. [22,24] suggest that the magnetic fields generated in coils should be at the order of hundreds of tesla, direct and accurate measurement demands further investigation. Our work can be utilized in MAFI schemes, such as the DCI scheme, the laboratory astrophysics involved with magnetized plasma jet, and magnetically guiding of REB.

ACKNOWLEDGMENTS

This work was supported by the Strategic Priority Research Program of Chinese Academy of Sciences (Grants No. XDA25050300, No. XDA25010300, and No. XDA25010100), the National Key R&D Program of China (Grant No. 2018YFA0404801), and National Natural Science Foundation of China (Grant No. 11827807).

APPENDIX A: SELF-CONSISTENT BOUNDARY CONDITION

Defining the inner product of the functions (scalar or vectorial) f, g on a spherical surface as in Eq. (A1), the normalized spherical harmonic function $Y_l^m(\theta,\varphi)$ has the form of Eq. (A2), where $P_l^m(x)$ is the associated Legendre function. With Wigner-3J symbols, the vector spherical harmonics can be defined by Eq. (A3) [68],

$$\langle f|g\rangle \equiv \frac{1}{4\pi}\oiint f\cdot g^* d\Omega, \tag{A1}$$

$$Y_l^m(\theta,\varphi) \equiv \sqrt{\frac{(l-m)!}{(l+m)!}(2l+1)}(-1)^m P_l^m(\cos\theta)e^{\mathbb{i}m\varphi}, \tag{A2}$$

$$\mathbf{Y}_{l,l_1}^m \equiv (-1)^{l-m}\sqrt{2l+1}\sum_{m_1,\mu}\begin{pmatrix} l & l_1 & 1\\ m & -m_1 & -\mu\end{pmatrix}Y_{l_1}^{m_1}\hat{\mathbf{e}}_\mu, \tag{A3}$$

where $\mu = 0, \pm 1$ and $l_1 = l, l\pm 1$. The complex vectors $\hat{\mathbf{e}}_\mu$ have the forms of $\hat{\mathbf{e}}_0 \equiv \hat{\mathbf{e}}_z, \hat{\mathbf{e}}_{\pm 1} \equiv -(\mathbb{i}\hat{\mathbf{e}}_y \pm \hat{\mathbf{e}}_x)/\sqrt{2}$. Here $(x,y,z) = (r\sin\theta\cos\varphi, r\sin\theta\sin\varphi, r\cos\theta)$. Radial differential operators $\partial_l^{l+1} \equiv \partial_r - l/r$, $\partial_l^{l-1} \equiv \partial_r + (l+1)/r$, and $D_l \equiv \partial_r^2 + (2/r)\partial_r - l(l+1)/r^2$ are introduced and part of the differential properties of spherical harmonics are listed here where we note $Y_\alpha \equiv Y_{l_\alpha}^{m_\alpha}$ and $\mathbf{Y}_\alpha \equiv \mathbf{Y}_{l_\alpha,l_{1\alpha}}^{m_\alpha}$ for short,

$$\langle Y_\alpha|Y_\beta\rangle = \delta_{\alpha\beta} \equiv \delta_{l_\alpha l_\beta}\delta_{m_\alpha m_\beta}, \tag{A4a}$$

$$\langle \mathbf{Y}_\alpha|\mathbf{Y}_\beta\rangle = \delta_{\alpha\beta} \equiv \delta_{l_\alpha l_\beta}\delta_{m_\alpha m_\beta}\delta_{l_{1\alpha}l_{1\beta}}, \tag{A4b}$$

$$\mathbf{Y}_{l,l}^m = \frac{\mathbb{i}\left(\hat{\mathbf{e}}_\theta \csc\theta\partial_\varphi Y_l^m - \hat{\mathbf{e}}_\varphi\partial_\theta Y_l^m\right)}{\sqrt{l(l+1)}}, \tag{A4c}$$

$$\nabla\left(fY_l^m\right) = \sqrt{\frac{l}{2l+1}}\mathbf{Y}_{l,l-1}^m\partial_l^{l-1}f - \sqrt{\frac{l+1}{2l+1}}\mathbf{Y}_{l,l+1}^m\partial_l^{l+1}f, \tag{A4d}$$

$$\nabla\times\left(f\mathbf{Y}_{l,l}^m\right) = \mathbb{i}\sqrt{\frac{l+1}{2l+1}}\mathbf{Y}_{l,l-1}^m\partial_l^{l-1}f + \mathbb{i}\sqrt{\frac{l}{2l+1}}\mathbf{Y}_{l,l+1}^m\partial_l^{l+1}f, \tag{A4e}$$

$$\nabla^2\left(fY_l^m\right) = Y_l^m D_l f. \tag{A4f}$$

Under the definition of vector spherical harmonics, the $\mathbf{Y}$-form of the field at infinity is $\mathbf{H}_\infty(t) = H_\infty(t)(\mathbf{Y}_{1,0}^{-1} - \mathbf{Y}_{1,0}^1)/\sqrt{2}$. We can derive the spherical harmonic spectrum form of boundary condition $\mathbf{H}^{(e)} = \mathbf{H}^{(i)}$ at $r = a$, expressing the field with TPD in Eq. (7) inside SDP and scalar potential outside:

$$\begin{aligned} &H_\infty(t)\frac{\mathbf{Y}_{1,0}^{-1} - \mathbf{Y}_{1,0}^1}{\sqrt{2}} - \sum_{l,m}\left[\sqrt{\frac{l}{2l+1}}\mathbf{Y}_{l,l-1}^m\partial_l^{l-1}\phi_l^m - \sqrt{\frac{l+1}{2l+1}}\mathbf{Y}_{l,l+1}^m\partial_l^{l+1}\phi_l^m\right]\\ &= \sum_{l,m}\left[(l+1)\sqrt{\frac{l}{2l+1}}\mathbf{Y}_{l,l-1}^m\partial_l^{l-1}S_l^m + l\sqrt{\frac{l+1}{2l+1}}\mathbf{Y}_{l,l+1}^m\partial_l^{l+1}S_l^m\right] - \sum_{l,m}\mathbb{i}\sqrt{l(l+1)}\mathbf{Y}_{l,l}^m T_l^m. \end{aligned} \tag{A5}$$

The vector spherical harmonics are orthonormal vectors, so Eq. (A5) requires $T_l^m(r=a) \equiv 0$. For S_l^ms, after some algebras we will get:

$$\partial_l^{l+1}\left[\phi_l^m - lS_l^m\right]_{r=a} = 0 \tag{A6a}$$

$$\sqrt{\frac{l}{2l+1}}\partial_l^{l-1}\left[\phi_l^m+(l+1)S_l^m\right]_{r=a}=\begin{cases}0, & (l,m)\neq(1,\pm1)\\ -\frac{mH_\infty(t)}{\sqrt{2}}, & (l,m)=(1,\pm1)\end{cases}. \tag{A6b}$$

Since the scalar potential obeys Laplace equation $\nabla^2\phi=0$, with the assistance of (A4f), the general solutions of coefficients have the form shown in Eq. (A7),

$$Y_l^m\left[\frac{\partial^2}{\partial r^2}+\frac{2}{r}\frac{\partial}{\partial r}-\frac{l(l+1)}{r^2}\right]\phi_l^m=0\quad \phi_l^m(r,t)=\frac{C_l^m(t)}{r^{l+1}}, \tag{A7}$$

where the positive power term has been omitted because of the boundary condition of $r\to+\infty$. Combining Eq. (A7), (A6a), and (A6b), the scalar potential term can be eliminated and the boundary conditions in Eqs. (9a) and (9b) are finally obtained.

APPENDIX B: EXPLICIT FORM OF SIMPLIFIED BULLARD-GELLMAN EQUATION

When the velocity field $\mathbf{u}(\mathbf{r})=u\hat{\mathbf{e}}_z$ is identical, the interaction terms on the right-hand side of Bullard-Gellman equations (8a) and (8b) can be simplified as Eq. (B1), where $\wp_\gamma=l_\gamma(l_\gamma+1)$

$$\begin{aligned}(\partial_t-\eta D_\gamma)S_\gamma&=\sum_\beta\left[\left(\vartheta_1^0,S_\beta,S_\gamma\right)+\left(\vartheta_1^0,T_\beta,S_\gamma\right)\right]\\ (\partial_t-\eta D_\gamma)T_\gamma&=\sum_\beta\left[\left(\vartheta_1^0,S_\beta,T_\gamma\right)+\left(\vartheta_1^0,T_\beta,T_\gamma\right)\right],\end{aligned} \tag{B1}$$

where

$$\begin{aligned}8\pi\wp_\gamma r^2(\vartheta_\alpha,S_\beta,S_\gamma)&=[-\wp_\alpha(-\wp_\alpha+\wp_\beta+\wp_\gamma)\vartheta_\alpha(rS_\beta)'+\wp_\beta(\wp_\alpha-\wp_\beta+\wp_\gamma)(r\vartheta_\alpha)'S_\beta]A_{\alpha\beta\gamma^*};\\ 4\pi\wp_\gamma r(\vartheta_\alpha,T_\beta,S_\gamma)&=\wp_\alpha\vartheta_\alpha T_\beta E_{\alpha\beta\gamma^*};\\ 4\pi\wp_\gamma r^3(\vartheta_\alpha,S_\beta,T_\gamma)&=[(\wp_\alpha+\wp_\beta+\wp_\gamma)\vartheta_\alpha S_\beta-(\wp_\alpha+\wp_\beta-\wp_\gamma)(r\vartheta_\alpha'S_\beta+r\vartheta_\alpha S_\beta'+r^2\vartheta_\alpha'S_\beta')-\wp_\alpha r^2\vartheta_\alpha S_\beta''-\wp_\beta r^2\vartheta_\alpha{}''S_\beta]E_{\alpha\beta\gamma^*};\\ 8\pi\wp_\gamma r^2(\vartheta_\alpha,T_\beta,T_\gamma)&=[\wp_\alpha(\wp_\alpha-\wp_\beta-\wp_\gamma)(r\vartheta_\alpha'T_\beta+r\vartheta_\alpha T_\beta')-\wp_\gamma(\wp_\alpha+\wp_\beta-\wp_\gamma)(\vartheta_\alpha T_\beta+r\vartheta_\alpha'T_\beta)]A_{\alpha\beta\gamma^*};\\ A_{\alpha\beta\gamma^*}&=(-1)^{m_\gamma}4\pi\Lambda_{\alpha\beta\gamma}\begin{pmatrix}l_\alpha & l_\beta & l_\gamma\\ 0 & 0 & 0\end{pmatrix}\begin{pmatrix}l_\alpha & l_\beta & l_\gamma\\ m_\alpha & m_\beta & -m_\gamma\end{pmatrix};\\ E_{\alpha\beta\gamma^*}&=-(-1)^{m_\gamma}4\pi\mathbb{i}\Lambda_{\alpha\beta\gamma}\Delta_{\alpha\beta\gamma}\begin{pmatrix}l_\alpha+1 & l_\beta+1 & l_\gamma+1\\ 0 & 0 & 0\end{pmatrix}\begin{pmatrix}l_\alpha & l_\beta & l_\gamma\\ m_\alpha & m_\beta & -m_\gamma\end{pmatrix};\\ \Lambda_{\alpha\beta\gamma}&=\sqrt{(2l_\alpha+1)(2l_\beta+1)(2l_\gamma+1)};\\ \Delta_{\alpha\beta\gamma}&=\sqrt{\frac{(l_\alpha+l_\beta+l_\gamma+2)(l_\alpha+l_\beta+l_\gamma+4)}{4(l_\alpha+l_\beta+l_\gamma+3)}}\sqrt{(l_\alpha+l_\beta-l_\gamma+1)(l_\beta+l_\gamma-l_\alpha+1)(l_\gamma+l_\alpha-l_\beta+1)}.\end{aligned}$$

The signs $A_{\alpha\beta\gamma^*}$ and $E_{\alpha\beta\gamma^*}$ represent for Adams-Gaunt integral and Elsasser dynamo integral separately [57,69]. When $\vartheta_\alpha\equiv\vartheta_0^1=ur/2\sqrt{3}$, $l_\alpha\equiv1$, $\wp_\alpha=2$, and $m_\alpha\equiv0$, the 3J symbols in $A_{\alpha\beta\gamma^*}$ and $E_{\alpha\beta\gamma^*}$ can be further simplified. Nonzero values of both $A_{\alpha\beta\gamma^*}$ and $E_{\alpha\beta\gamma^*}$ require that $m_\beta=m_\gamma=m$, and $l_\beta=l_\gamma,l_\gamma\pm1$. Moreover, $E_{\alpha\beta\gamma^*}$ and $A_{\alpha\beta\gamma^*}$ will not be nonzero at the same time due to the first 3J symbol in their expressions. The further calculation gives the interaction forms for each spectrum equation in Eq. (B2)–(B4) as follows:

(a) $l_\beta=l_\gamma+1$:

$$\begin{aligned}(\vartheta_1^0,S_\beta,S_\gamma)&=-u\frac{l_\gamma+2}{l_\gamma+1}\sqrt{\frac{(l_\gamma+1)^2-m^2}{4(l_\gamma+1)^2-1}}\left[(l_\gamma+2)\frac{S_\beta(r)}{r}+S_\beta'(r)\right]\\ (\vartheta_1^0,T_\beta,S_\gamma)&=0\\ (\vartheta_1^0,S_\beta,T_\gamma)&=0\\ (\vartheta_1^0,T_\beta,T_\gamma)&=-u\frac{l_\gamma+2}{l_\gamma+1}\sqrt{\frac{(l_\gamma+1)^2-m^2}{4(l_\gamma+1)^2-1}}\left[(l_\gamma+2)\frac{T_\beta(r)}{r}+T_\beta'(r)\right],\end{aligned} \tag{B2}$$

(b) $l_\beta = l_\gamma$:

$$
\begin{aligned}
&(\mathcal{I}_1^0, S_\beta, S_\gamma) = 0\\
&(\mathcal{I}_1^0, T_\beta, S_\gamma) = -\mathbb{i}um\frac{T_\beta(r)}{l_\gamma(l_\gamma+1)}\\
&(\mathcal{I}_1^0, S_\beta, T_\gamma) = \mathbb{i}um\left[\frac{1}{l_\gamma(l_\gamma+1)}S_\beta''(r) + \frac{2}{l_\gamma(l_\gamma+1)}\frac{S_\beta'(r)}{r} - \frac{S_\beta(r)}{r^2}\right]\\
&(\mathcal{I}_1^0, T_\beta, T_\gamma) = 0,
\end{aligned}
\tag{B3}
$$

(c) $l_\beta = l_\gamma + 1$:

$$
\begin{aligned}
&\left(\mathcal{I}_1^0, S_\beta, S_\gamma\right) = u\frac{l_\gamma-1}{l_\gamma}\sqrt{\frac{l_\gamma^2-m^2}{4l_\gamma^2-1}}\left[(l_\gamma-1)\frac{S_\beta(r)}{r} - S_\beta'(r)\right]\\
&\left(\mathcal{I}_1^0, T_\beta, S_\gamma\right) = 0\\
&\left(\mathcal{I}_1^0, S_\beta, T_\gamma\right) = 0\\
&\left(\mathcal{I}_1^0, T_\beta, T_\gamma\right) = u\frac{l_\gamma-1}{l_\gamma}\sqrt{\frac{l_\gamma^2-m^2}{4l_\gamma^2-1}}\left[(l_\gamma-1)\frac{T_\beta(r)}{r} - T_\beta'(r)\right].
\end{aligned}
\tag{B4}
$$

Let $\mathcal{T}_\gamma \equiv \mathbb{i}T_\gamma$, and (B1) becomes a set of real scalar variable cascade equations. The prerequisite $m_\beta = m_\gamma = m$ indicates that coefficients with different m values are decoupled. According to the boundary conditions (9a) and (9b) and all-zero initial value, only coefficients with a superscript of $m = \pm 1$ have nontrivial evolution behavior, leading to the cascade structure given in Fig. 2. With a truncation of l, the numerical method can be applied to solving such a coupled system.

[1] M. Tabak, J. Hammer, M. E. Glinsky, W. L. Kruer, S. C. Wilks, J. Woodworth, E. M. Campbell, M. D. Perry, and R. J. Mason, Ignition and high gain with ultrapowerful lasers, Phys. Plasmas **1**, 1626 (1994).

[2] R. Kodama, P. A. Norreys, K. Mima, A. E. Dangor, R. G. Evans, H. Fujita, Y. Kitagawa, K. Krushelnick, T. Miyakoshi, N. Miyanaga, T. Norimatsu, S. J. Rose, T. Shozaki, K. Shigemori, A. Sunahara, M. Tampo, K. A. Tanaka, Y. Toyama, T. Yamanaka, and M. Zepf, Fast heating of ultrahigh-density plasma as a step towards laser fusion ignition, Nature (London) **412**, 798 (2001).

[3] M. Tabak, D. Hinkel, S. Atzeni, E. M. Campbell, and K. Tanaka, Fast ignition: Overview and background, Fusion Sci. Technol. **49**, 254 (2006).

[4] A. R. Piriz and M. M. Sánchez, Analytic model for the dynamics of fast ignition, Phys. Plasmas **5**, 2721 (1998).

[5] S. Atzeni, Inertial fusion fast ignitor: Igniting pulse parameter window vs the penetration depth of the heating particles and the density of the precompressed fuel, Phys. Plasmas **6**, 3316 (1999).

[6] N. G. Basov, S. Y. Gus'kov, and L. P. Feokistov, Thermonuclear gain of ICF targets with direct heating of ignitor, J. Sov. Laser Res. **13**, 396 (1992).

[7] H. Nagatomo, T. Johzaki, T. Asahina, M. Hata, Y. Sentoku, K. Mima, and H. Sakagami, Study of fast ignition target design for ignition and burning experiments, Nucl. Fusion **59**, 106055 (2019).

[8] M. H. Key, J. C. Adam, K. U. Akli, M. Borghesi, M. H. Chen, R. G. Evans, R. R. Freeman, H. Habara, S. P. Hatchett, J. M. Hill, A. Heron, J. A. King, R. Kodama, K. L. Lancaster, A. J. MacKinnon, P. Patel, T. Phillips, L. Romagnani, R. A. Snavely, R. Stephens *et al.*, Fast ignition relevant study of the flux of high intensity laser-generated electrons via a hollow cone into a laser-imploded plasma, Phys. Plasmas **15**, 022701 (2008).

[9] A. G. MacPhee, L. Divol, A. J. Kemp, K. U. Akli, F. N. Beg, C. D. Chen, H. Chen, D. S. Hey, R. J. Fedosejevs, R. R. Freeman, M. Henesian, M. H. Key, S. Le Pape, A. Link, T. Ma, A. J. MacKinnon, V. M. Ovchinnikov, P. K. Patel, T. W. Phillips, R. B. Stephens *et al.*, Limitation on Prepulse Level Forcone-Guided Fast-Ignition Inertial Confinement Fusion, Phys. Rev. Lett. **104**, 055002 (2010).

[10] W. Theobald, A. A. Solodov, C. Stoeckl, K. S. Anderson, R. Betti, T. R. Boehly, R. S. Craxton, J. A. Delettrez, C. Dorrer, J. A. Frenje, V. Y. Glebov, H. Habara, K. A. Tanaka, J. P. Knauer, R. Lauck, F. J. Marshall, K. L. Marshall, D. D. Meyerhofer, P. M. Nilson, P. K. Patel *et al.*, Initial cone-in-shell fast-ignition experiments on OMEGA, Phys. Plasmas **18**, 056305 (2011).

[11] H. Shiraga, S. Fujioka, M. Nakai, T. Watari, H. Nakamura, Y. Arikawa, H. Hosoda, T. Nagai, M. Koga, H. Kikuchi, Y. Ishii, T. Sogo, K. Shigemori, H. Nishimura, Z. Zhang, M. Tanabe, S. Ohira, Y. Fujii, T. Namimoto, Y. Sakawa *et al.*, Fast ignition integrated experiments with Gekko and LFEX lasers, Plasma Phys. Controlled Fusion **53**, 124029 (2011).

[12] A. Rousse, P. Audebert, J. P. Geindre, F. Falliès, J. C. Gauthier, A. Mysyrowicz, G. Grillon, and A. Antonetti, Efficient K x-ray source from femtosecond laser-produced plasmas, Phys. Rev. E **50**, 2200 (1994).

[13] C. Reich, P. Gibbon, I. Uschmann, and E. Förster, Yield Optimization and Time Structure of Femtosecond Laser Plasma $K\alpha$ Sources, Phys. Rev. Lett. **84**, 4846 (2000).

[14] L. M. Chen, M. Kando, M. H. Xu, Y. T. Li, J. Koga, M. Chen, H. Xu, X. H. Yuan, Q. L. Dong, Z. M. Sheng, S. V. Bulanov, Y. Kato, J. Zhang, and T. Tajima, Study of X-Ray Emission

Enhancement Via a High-Contrast Femtosecond Laser Interacting with a Solid Foil, Phys. Rev. Lett. **100**, 045004 (2008).

[15] S. Sander, T. Ebert, D. Hartnagel, M. Hesse, X. Pan, G. Schaumann, M. Šmíd, K. Falk, and M. Roth, Microstructured layered targets for improved laser-induced x-ray backlighters, Phys. Rev. E **104**, 065207 (2021).

[16] M. J. Berger and S. M. Seltzer, Bremsstrahlung and photoneutrons from thick tungsten and tantalum targets, Phys. Rev. C **2**, 621 (1970).

[17] X. R. Jiang, D. B. Zou, Z. J. Zhao, L. X. Hu, P. Han, J. Q. Yu, T. P. Yu, Y. Yin, and F. Q. Shao, Microstructure-assisted laser-driven photonuclear pulsed neutron source, Phys. Rev. Appl. **15**, 034032 (2021).

[18] L. M. Chen, M. Kando, J. Ma, H. Kotaki, Y. Fukuda, Y. Hayashi, I. Daito, T. Homma, K. Ogura, M. Mori, A. S. Pirozhkov, J. Koga, H. Daido, S. V. Bulanov, T. Kimura, T. Tajima, and Y. Kato, Phase-contrast x-ray imaging with intense Ar Kα radiation from femtosecond-laser-driven gas target, Appl. Phys. Lett. **90**, 211501 (2007).

[19] S. Kahaly, S. K. Yadav, W. M. Wang, S. Sengupta, Z. M. Sheng, A. Das, P. K. Kaw, and G. R. Kumar, Near-Complete Absorption of Intense, Ultrashort Laser Light by Sub-λ Gratings, Phys. Rev. Lett. **101**, 145001 (2008).

[20] W. M. Wang, P. Gibbon, Z. M. Sheng, and Y. T. Li, Magnetically Assisted Fast Ignition, Phys. Rev. Lett. **114**, 015001 (2015).

[21] D. J. Strozzi, M. Tabak, D. J. Larson, L. Divol, A. J. Kemp, C. Bellei, M. M. Marinak, and M. H. Key, Fast-ignition transport studies: Realistic electron source, integrated particle-in-cell and hydrodynamic modeling, imposed magnetic fields, Phys. Plasmas **19**, 072711 (2012).

[22] M. Bailly-Grandvaux, J. J. Santos, C. Bellei, P. Forestier-Colleoni, S. Fujioka, L. Giuffrida, J. J. Honrubia, D. Batani, R. Bouillaud, M. Chevrot, J. E. Cross, R. Crowston, S. Dorard, J. L. Dubois, M. Ehret, G. Gregori, S. Hulin, S. Kojima, E. Loyez, J. R. Marquès *et al.*, Guiding of relativistic electron beams in dense matter by laser-driven magnetostatic fields, Nat. Commun. **9**, 102 (2018).

[23] E. M. Epperlein and M. G. Haines, Plasma transport coefficients in a magnetic field by direct numerical solution of the Fokker-Planck equation, Phys. Fluids **29**, 1029 (1986).

[24] S. Sakata, S. Lee, H. Morita, T. Johzaki, H. Sawada, Y. Iwasa, K. Matsuo, K. F. F. Law, A. Yao, M. Hata, A. Sunahara, S. Kojima, Y. Abe, H. Kishimoto, A. Syuhada, T. Shiroto, A. Morace, A. Yogo, N. Iwata, M. Nakai *et al.*, Magnetized fast isochoric laser heating for efficient creation of ultra-high-energy-density states, Nat. Commun. **9**, 3937 (2018).

[25] T. Taguchi, T. M. Antonsen Jr., and K. Mima, Electron beam propagation and magnetic structure formation in a strongly magnetized, collisional plasma, High Energy Density Phys. **37**, 100881 (2020).

[26] T. Sano, Y. Tanaka, N. Iwata, M. Hata, K. Mima, M. Murakami, and Y. Sentoku, Broadening of cyclotron resonance conditionsin the relativistic interaction of an intense laser with overdense plasmas, Phys. Rev. E **96**, 043209 (2017).

[27] H. H. Song, W. M. Wang, J. Q. Wang, Y. T. Li, and J. Zhang, Low-frequency whistler waves excited by relativisticaser pulses, Phys. Rev. E **102**, 053204 (2020).

[28] S. X. Luan, W. Yu, F. Y. Li, D. Wu, Z. M. Sheng, M. Y. Yu, and J. Zhang, Laser propagation in dense magnetized plasma, Phys. Rev. E **94**, 053207 (2016).

[29] T. Sano, M. Hata, D. Kawahito, K. Mima, and Y. Sentoku, Ultrafast wave-particle energy transfer in the collapse of standing whistler waves, Phys. Rev. E **100**, 053205 (2019).

[30] T. Sano, S. Fujioka, Y. Mori, K. Mima, and Y. Sentoku, Thermonuclear fusion triggered by collapsing standing whistler waves in magnetized overdense plasmas, Phys. Rev. E **101**, 013206 (2020).

[31] T. Johzaki, M. Hino, M. Horio, S. Takeda, W. Kim, T. Endo, S. Fujioka, Y. Sentoku, H. Nagatomo, and A. Sunahara, Intensification of laser-produced relativistic electron beam using converging magnetic fields for ignition in fast ignition laser fusion, High Energy Density Phys. **36**, 100841 (2020).

[32] M. A. Liberman and A. L. Velikovich, On the ignition of a self-sustained fusion reaction in a dense DT plasma, J. Plasma Phys. **31**, 381 (1984).

[33] O. V. Gotchev, P. Y. Chang, J. P. Knauer, D. D. Meyerhofer, O. Polomarov, J. Frenje, C. K. Li, M. J. Manuel, R. D. Petrasso, J. R. Rygg, F. H. Séguin, and R. Betti, Laser-Driven Magnetic-Flux Compression in High-Energy-Density Plasmas, Phys. Rev. Lett. **103**, 215004 (2009).

[34] M. Hohenberger, P. Y. Chang, G. Fiksel, J. P. Knauer, R. Betti, F. J. Marshall, D. D. Meyerhofer, F. H. Séguin, and R. D. Petrasso, Inertial confinement fusion implosions with imposed magnetic field compression using the OMEGA Laser, Phys. Plasmas **19**, 056306 (2012).

[35] D. Kawahito, M. Bailly-Grandvaux, M. Dozières, C. McGuffey, P. Forestier-Colleoni, J. Peebles, J. J. Honrubia, B. Khiar, S. Hansen, P. Tzeferacos, M. S. Wei, C. M. Krauland, P. Gourdain, J. R. Davies, K. Matsuo, S. Fujioka, E. M. Campbell, J. J. Santos, D. Batani, K. Bhutwala *et al.*, Fast electron transport dynamics and energy deposition in magnetized, imploded cylindrical plasma: Electron transport in magnetized plasmas, Philos. Trans. R. Soc. A **379**, 0 (2021).

[36] M. Dozières, S. Hansen, P. Forestier-Colleoni, C. McGuffey, D. Kawahito, M. Bailly-Grandvaux, K. Bhutwala, C. M. Krauland, M. S. Wei, P. Gourdain, J. R. Davies, K. Matsuo, S. Fujioka, E. M. Campbell, J. L. Peebles, J. J. Santos, D. Batani, S. Zhang, and F. N. Beg, Characterization of an imploding cylindrical plasma for electron transport studies using x-ray emission spectroscopy, Phys. Plasmas **27**, 023302 (2020).

[37] S. Fujioka, Y. Arikawa, S. Kojima, T. Johzaki, H. Nagatomo, H. Sawada, S. H. Lee, T. Shiroto, N. Ohnishi, A. Morace, X. Vaisseau, S. Sakata, Y. Abe, K. Matsuo, K. F. Farley Law, S. Tosaki, A. Yogo, K. Shigemori, Y. Hironaka, Z. Zhang *et al.*, Fast ignition realization experiment with high-contrast kilo-joule peta-watt LFEX laser and strong external magnetic field, Phys. Plasmas **23**, 056308 (2016).

[38] E. C. Hansen, J. R. Davies, D. H. Barnak, R. Betti, E. M. Campbell, V. Y. Glebov, J. P. Knauer, L. S. Leal, J. L. Peebles, A. B. Sefkow, and K. M. Woo, Neutron yield enhancement and suppression by magnetization in laser-driven cylindrical implosions, Phys. Plasmas **27**, 062703 (2020).

[39] J. D. Moody, B. B. Pollock, H. Sio, D. J. Strozzi, D. D. Ho, C. Walsh, G. E. Kemp, S. O. Kucheyev, B. Kozioziemski, E. G. Carroll, J. Kroll, D. K. Yanagisawa, J. Angus, S. D. Bhandarkar, J. D. Bude, L. Divol, B. Ferguson, J. Fry, L. Hagler, E. Hartouni *et al.*, The magnetized indirect drive project on the National Ignition Facility, J. Fusion Energy **41**, 7(2022).

[40] C. A. Walsh, R. Florido, M. Bailly-Grandvaux, F. Suzuki-Vidal, J. P. Chittenden, A. J. Crilly, M. A. Gigosos, R. C. Mancini, G. Pérez-Callejo, C. Vlachos, C. McGuffey, F. N. Beg, and J. J. Santos, Exploring extreme magnetization phenomena in directly driven imploding cylindrical targets, Plasma Phys. Control. Fusion **64**, 025007 (2022).

[41] C. A. Walsh, S. O'Neill, J. P. Chittenden, A. J. Crilly, B. Appelbe, D. J. Strozzi, D. Ho, H. Sio, B. Pollock, L. Divol, E. Hartouni, M. Rosen, B. G. Logan, and J. D. Moody, Magnetized ICF implosions: Scaling of temperature and yield enhancement, Phys. Plasmas **29**, 042701 (2022).

[42] A. Bose, J. Peebles, C. A. Walsh, J. A. Frenje, N. V. Kabadi, P. J. Adrian, G. D. Sutcliffe, M. Gatu Johnson, C. A. Frank, J. R. Davies, R. Betti, V. Y. Glebov, F. J. Marshall, S. P. Regan, C. Stoeckl, E. M. Campbell, H. Sio, J. Moody, A. Crilly, B. D. Appelbe *et al.*, Effect of Strongly Magnetized Electrons and Ions on Heat Flow and Symmetry of Inertial Fusion Implosions, Phys. Rev. Lett. **128**, 195002 (2022).

[43] K. Matsuo, T. Sano, H. Nagatomo, T. Somekawa, King Fai Fairley Law, H. Morita, Y. Arikawa, and S. Fujioka, Enhancement of Ablative Rayleigh-Taylor Instability Growth by Thermal Conduction Suppression in a Magnetic Field, Phys. Rev. Lett. **127**, 165001 (2021).

[44] C. A. Walsh, Magnetized ablative Rayleigh-Taylor instability in three dimensions, Phys. Rev. E **105**, 025206 (2022).

[45] C. Walsh, A. Crilly, and J. Chittenden, Magnetized directly-driven ICF capsules: increased instability growth from non-uniform laser drive, Nucl. Fusion **60**, 106006 (2020).

[46] J. Zhang, W. M. Wang, X. H. Yang, D. Wu, Y. Y. Ma, J. L. Jiao, Z. Zhang, F. Y. Wu, X. H. Yuan, Y. T. Li, and J. Q. Zhu, Double-cone ignition scheme for inertial confinement fusion, Philos. Trans. R. Soc. A **378**, 20200015 (2020).

[47] H. Azechi, T. Sakaiya, T. Watari, M. Karasik, H. Saito, K. Ohtani, K. Takeda, H. Hosoda, H. Shiraga, M. Nakai, K. Shigemori, S. Fujioka, M. Murakami, H. Nagatomo, T. Johzaki, J. Gardner, D. G. Colombant, J. W. Bates, A. L. Velikovich, Y. Aglitskiy *et al.*, Experimental Evidence of Impact Ignition: 100-Fold Increase of Neutron Yield by Impactor Collision, Phys. Rev. Lett. **102**, 235002 (2009).

[48] L. Landau and E. Lifshitz, Quasi-static electromagnetic rield, in *Electrodynamics of Continuous Media*, edited by L. D. Landau and E. M. Lifshitz (Pergamon, Amsterdam, 1984), Vol. 8, pp. 199–224

[49] S. Fujioka, Z. Zhang, K. Ishihara, K. Shigemori, Y. Hironaka, T. Johzaki, A. Sunahara, N. Yamamoto, H. Nakashima, T. Watanabe, H. Shiraga, H. Nishimura, and H. Azechi, Kilotesla magnetic field due to a capacitor-coil target driven by high power laser, Sci. Rep. **3**, 1 (2013).

[50] H.-b. Tang, G.-y. Hu, Y.-h. Liang, T. Tao, Y.-l. Wang, P. Hu, B. Zhao, and J. Zheng, Confinement of laser plasma expansion with strong external magnetic field, Plasma Phys. Control. Fusion **60**, 055005 (2018).

[51] H. Morita, T. Ogitsu, F. R. Graziani, and S. Fujioka, Advanced analysis of laser-driven pulsed magnetic diffusion based on quantum molecular dynamics simulation, Matter Radiat. Extremes **6**, 065901 (2021).

[52] R. S. Cohen, L. Spitzer, and P. M. Routly, The electrical conductivity of an ionized gas, Phys. Rev. **80**, 230 (1950).

[53] Setsuo Ichimaru, *Statistical Physics of Dense Plasmas: Elementary Processes and Phase Transitions*, 1st ed. (Chapman & Hall/CRC, London, 2019).

[54] G. Rousseaux, Forty years of Galilean Electromagnetism (1973-2013), Eur. Phys. J. Plus **128**, 81 (2013).

[55] C. A. Walsh, J. D. Sadler, and J. R. Davies, Updated magnetized transport coefficients: Impact on laser-plasmas with self-generated or applied magnetic fields, Nucl. Fusion **61**, 116025 (2021).

[56] J. D. Sadler, H. Li, and K. A. Flippo, Parameter space for magnetization effects in high-energy-density plasmas, Matter Radiat. Extremes **6**, 065902 (2021).

[57] D. J. Ivers and C. G. Phillips, Scalar and vector spherical harmonic spectral equations of rotating magnetohydrodynamics, Geophys. J. Int. **175**, 955 (2008).

[58] E. Bullard and H. Gellman, Homogeneous dynamos and terrestrial magnetism, Philos. Trans. R. Soc. Lond. A **247**, 213 (1954).

[59] S. Ichimaru and S. Tanaka, Theory of interparticle correlations in dense, high-temperature plasmas. V. Electric and thermal conductivities, Phys. Rev. A **32**, 1790 (1985).

[60] Y. T. Lee and R. M. More, An electron conductivity model for dense plasmas, Phys. Fluids **27**, 1273 (1984).

[61] S. X. Hu, L. A. Collins, T. R. Boehly, Y. H. Ding, P. B. Radha, V. N. Goncharov, V. V. Karasiev, G. W. Collins, S. P. Regan, and E. M. Campbell, A review on *ab initio* studies of static, transport, and optical properties of polystyrene under extreme conditions for inertial confinement fusion applications, Phys. Plasmas **25**, 056306 (2018).

[62] M. French, G. Röpke, M. Schörner, M. Bethkenhagen, M. P. Desjarlais, and R. Redmer, Electronic transport coefficients from density functional theory across the plasma plane, Phys. Rev. E **105**, 065204 (2022).

[63] J. D. Sadler, H. Li, and K. A. Flippo, Magnetic field generation from composition gradients in inertial confinement fusion fuel, Philos. Trans. R. Soc. A **378**, 20200045(2020).

[64] J. L. Peebles, J. R. Davies, D. H. Barnak, T. Cracium, M. J. Bonino, and R. Betti, Axial proton probing of magnetic and electric fields inside laser-driven coils, Phys. Plasmas **27**, 063109 (2020).

[65] L. Gao, H. Ji, G. Fiksel, W. Fox, M. Evans, and N. Alfonso, Ultrafast proton radiography of the magnetic fields generated by a laser-driven coil current, Phys. Plasmas **23**, 043106 (2016).

[66] J. J. Santos, M. Bailly-Grandvaux, M. Ehret, A. V. Arefiev, D. Batani, F. N. Beg, A. Calisti, S. Ferri, R. Florido, P. Forestier-Colleoni, S. Fujioka, M. A. Gigosos, L. Giuffrida, L. Gremillet, J. J. Honrubia, S. Kojima, P. Korneev, K. F. Law, J. R. Marquès, A. Morace *et al.*, Laser-driven strong magnetostatic fields with applications to charged beam transport and magnetized high energy-density physics, Phys. Plasmas **25**, 056705 (2018).

[67] J. L. Peebles, J. R. Davies, D. H. Barnak, F. Garcia-Rubio, P. V. Heuer, G. Brent, R. Spielman, and R. Betti, An assessment of generating quasi-static magnetic fields using laser-driven "capacitor" coils, Phys. Plasmas **29**, 080501 (2022).

[68] R. W. James and A. H. Cook, The spectral form of the magnetic induction equation, Proc. R. Soc. Lond. A **340**, 287 (1974).

[69] R. W. James and A. H. Cook, The Adams and Elsasser dynamo integrals, Proc. R. Soc. Lond. A **331**, 469 (1973).